Journal of Materials Science & Technology 85 (2021) 44–55

Contents lists available at ScienceDirect

Journal of Materials Science & Technology

journal homepage: www.jmst.org

Reusable and durable electrostatic air filter based on hybrid metallized microfibers decorated with metal–organic–framework nanocrystals

Min-Woo Kim[a,b,1], Yong-Il Kim[a,1], Chanwoo Park[a], Ali Aldalbahi[c], Hamdah S. Alanazi[c], Seongpil An[b,d,*], Alexander L. Yarin[e,*], Sam S. Yoon[a,*]

[a] School of Mechanical Engineering, Korea University, Seoul 02841, Republic of Korea
[b] SKKU Advanced Institute of Nanotechnology (SAINT), Sungkyunkwan University (SKKU), Suwon 16419, Republic of Korea
[c] Department of Chemistry, College of Science, King Saud University, Riyadh 11451, Saudi Arabia
[d] Department of Nano Engineering, Sungkyunkhwan University (SKKU), Suwon 16419, Republic of Korea
[e] Department of Mechanical and Industrial Engineering, University of Illinois at Chicago, 842 W. Taylor St., Chicago, IL 60607-7022, USA

ARTICLE INFO

Article history:
Received 9 September 2020
Received in revised form
17 December 2020
Accepted 30 December 2020
Available online 9 February 2021

Keywords:
Electrospinning
Metallized microfibers
Metal organic framework (MOF) nanocrystals
Corona discharge
Reusable fibrous filter for air purification

ABSTRACT

As global air pollution becomes increasingly severe, various types of fibrous filters have been developed to improve air filter performance. However, fibrous filters have limitations such as high packing density that generally causes high-pressure drop and ultimately deterioration in the filtration efficiency. High-pressure particulate matter precipitators are limited in terms of scope for commercialization because they require high voltage supplies and ozone generators. In this study, we develop fibrous filters with enhanced durability and improved performance using metallized microfibers decorated with metal–organic-framework (MOF) nanocrystals. Not only does the efficiency of the developed filters remain at or above 97 % for 0.50–1.5 μm PMs but the durability also significantly increases. In addition, using the water purification ability of the MOF, we explore the dye degradation effect of the hybrid microfibers by immersing them into Rhodamine B aqueous solution. In such an experiment the Rhodamine B aqueous solution is completely purified by the presence of the hybrid microfibers under the UV irradiation.

1. Introduction

Although technological developments of human civilization, along with rapid industrialization, have led to greater comfort and convenience of life, the resulting environmental problems have caused significant threats to human beings in recent decades. Among various environmental issues, air pollution, especially that associated with particulate matter (PM), has recently become one of the most severe problems [1–10]. Atmospheric air pollution can be natural (dust or sand storms, volcano eruptions, large forest fires) or attributed to several anthropogenic factors, such as automobile usage, construction sites, and the growth of manufacturing industries. In addition to these external factors, air pollutants can be also generated in internal spaces where humans live (*e.g.*, fine polymer dust detached from fabrics and inorganic particles generated from airtight spaces such as subway stations, soot precipitation, *etc.*) [6,8,11].

Considering the seriousness of air pollution, research on air purification technology has progressed very quickly in recent years [5,6,8,12–17]. While various types of fibrous filters are being developed [16,18–20], research and development (R&D) on electrostatic precipitators (ESPs) in particular has been actively conducted to improve the air purification capabilities of existing fibrous filters [21–24]. Therefore, several studies demonstrating that the use of electric force in fibrous filters can improve their filtration efficiency have been published recently, and additional innovative studies for further efficiency enhancement are also underway [14–16,20]. Indeed, several studies have shown discernible improvements in the filtration efficiency of electrostatic fibrous filters because of the application of external electrostatic fields [16,25] or usage

* Corresponding authors.
E-mail addresses: esan@skku.edu (S. An), ayarin@uic.edu (A.L. Yarin), skyoon@korea.ac.kr (S.S. Yoon).
[1] These authors contributed equally to this work.

https://doi.org/10.1016/j.jmst.2020.12.065
1005-0302/

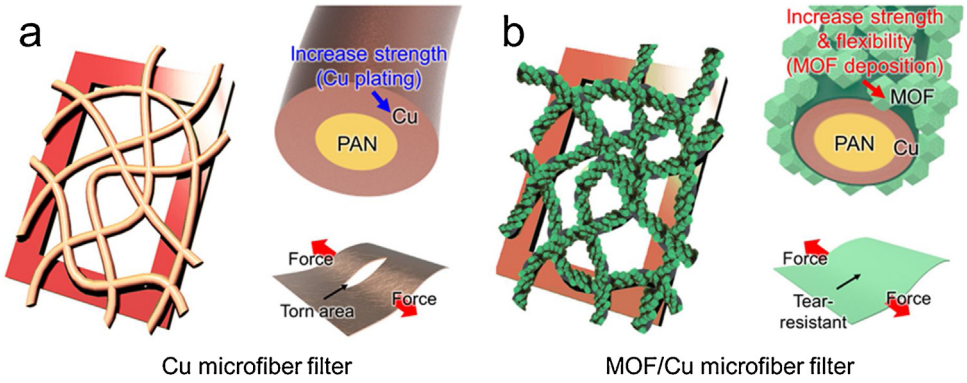

Fig. 1. Schematics of different fibrous filters based on (a) Cu microfibers and (b) MOF/Cu microfibers. Insets located in the bottom right of panels (a) and (b) illustrate the difference in durability between the Cu microfiber filter and the MOF/Cu microfiber filter loaded by external stresses.

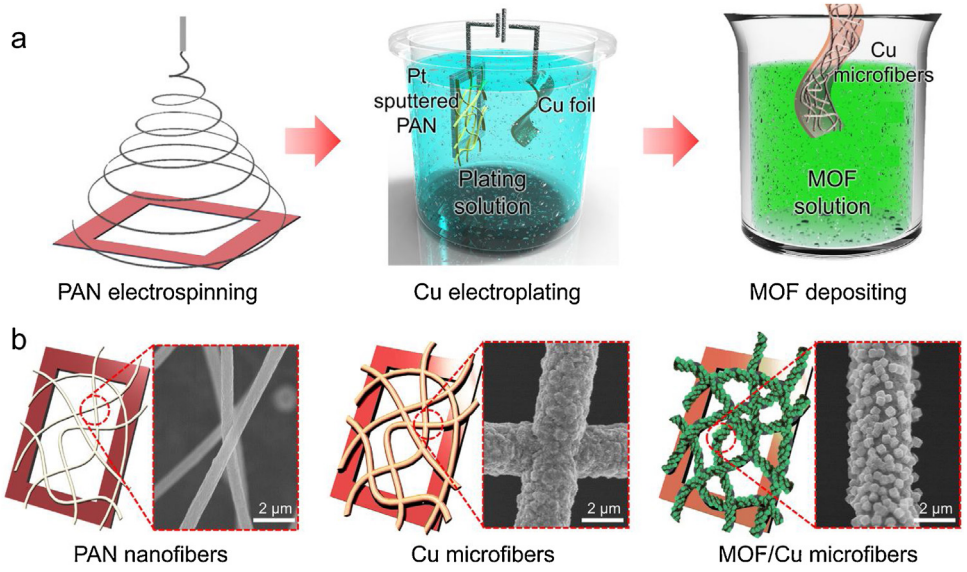

Fig. 2. (a) Fabrication process of the MOF/Cu microfibers, and (b) the corresponding illustrations and scanning electron microscopy (SEM) images after each stage of the process.

of ionization-related methods [12,13,26] for converting PM into unipolar ions.

For example, Shi et al. [13] demonstrated that the filtration efficiency of glass-fiber filters could be improved by up to 40 % via the introduction of an ionizer in front of the glass fibers. They also developed a sustainable method capable of maintaining at least 50 % filtration efficiency over half a year via periodical ionizer polarity-switching technique. In addition, Park et al. [12] performed a study which showed that filtration efficiency could be enhanced by up to 1.6 times (*i.e.*, from 16 % to 25 %) via the use of an ionizer on carbon fibers.

The present group has recently proposed a promising method to overcome the shortcomings of existing fibrous filters by introducing a combined approach to filtration employing electrostatic forces [16]. In that study, not only the high pressure-drop issue was overcome by minimizing the thickness of the developed fibrous filter, but also the reusability of the fiber filters was facilitated. Accordingly, the durability of high-efficiency metallized fibrous filters was significantly improved [16].

A metal–organic framework (MOF), comprising organic ligands linking metal ions or clusters, is a representative class of materials with significant sub-micrometer pores [27–32]. MOF-based filters have hitherto shown considerable potential for air purification and contaminant control because of their tunable porosity, large surface area benefiting gas adsorption, and good chemical and thermal stability [33–38]. In addition, MOF deposition onto polymer-based filters also improves mechanical strength, enabling the fiber-based filter to withstand high-speed flow [39], which indicates that it is possible to develop a mechanically improved sustainable filter via incorporation of MOFs into fibrous filters.

Herein, we fabricated fibrous filters exhibiting enhanced durability and improved performance using metallized microfibers and MOF nanocrystals, where the latter were decorated on the surfaces of the metallized microfibers via a MOF deposition method. The metallized fibers were formed via a combined technique of electrospinning and electroplating. The metal employed here to form metallized microfibers was copper (Cu). It was chosen due to the following three reasons. First, the Cu microfibers have reasonable mechanical properties that are required for filter applications (cf. Fig. 1) [40]. Second, Cu forms a strong physicochemical bond with zinc (Zn) ions in the MOF, which could prevent the MOF nanocrystals from separating from the Cu microfibers during filtration (cf. Fig. 2). Third, the high electrical conductivity of the Cu microfibers led to a high filtration efficiency of the filters by increasing electron transfer from the filtered (or captured) PM to an electrically grounded part of filters (cf. Fig. 3). Note also that Cu is one of the cost-effective and easy-to-manufacture metals. On the other hand, we also improved the filtration efficiency

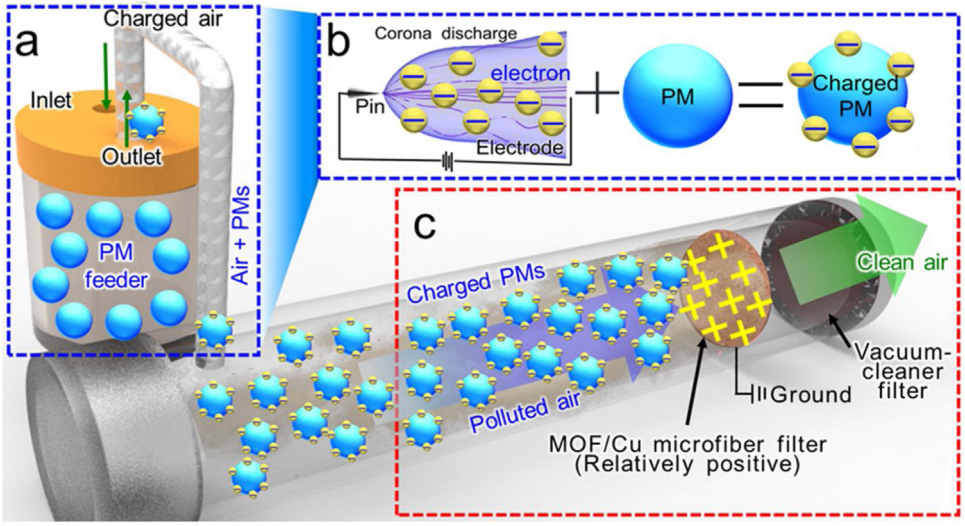

Fig. 3. Schematic of filtration test with MOF/Cu microfiber filter: (a) PM feeder wherein the ionized air and PM are mixed, (b) charging of PM by electrons in the ionized air, (c) filtration process in the MOF/Cu microfiber filter.

Table 1
Operating conditions for PAN electrospinning and Cu electroplating.

Process	Parameters	Values
Electrospinning	Applied DC voltage [kV]	6
	Flow rate [μl h^{-1}]	280
	Needle-to-collector distance [cm]	13
	Electrospinning time [s]	60
Electroplating	Applied DC voltage [kV]	3
	Nanofiber mat-to-Cu electrode distance [cm]	3
	Electroplating time [s]	60

via corona discharge ionization on the MOF-decorated metallized microfibers.

Fig. 1 displays the morphology and comparison of Cu microfibers and MOF-decorated Cu (MOF/Cu) microfibers. A Cu microfiber mats are formed by electroplating Cu layers on electrospun polyacrylonitrile (PAN) nanofiber mats (Fig. 1a). The MOF/Cu microfiber mats are obtained by depositing MOF on the Cu microfiber mats, which intends to improve both mechanical durability and filtration efficiency.

2. Experimental methods

2.1. Fabrication of MOF/Cu microfibers

The fabrication process for the metal–organic framework of (MOF)/copper (Cu) microfibers is illustrated in Fig. 2a. Note that all fabrication processes were carried out at the room temperature of 20–25 °C and the humidity of 30–40 RH%. MOF/Cu microfibers are fabricated via deposition of MOF onto Cu microfibers. The Cu microfibers are prepared via electrospinning employing 8 wt% of polyacrylonitrile (PAN, M_w =150 kDa, Sigma-Aldrich, USA) solution dissolved in *N*,*N*-dimethylformamide (DMF, 99.8 %, Sigma-Aldrich, USA), and electroplating employing a Cu-plating solution. Note that PAN nanofibers are just a support for making Cu microfibers, so other polymers capable of electrospinning can replace PAN. The operating conditions for the PAN electrospinning and Cu electroplating are listed in Table 1; further details associated with these processes can be found elsewhere [16,40–45]. The size and thickness of the PAN nanofiber mat were 5 cm × 5 cm and 2 μm, respectively. Prior to electroplating, Pt sputtering onto the surface of electrospun PAN nanofibers was used enabling the non-conductive PAN nanofibers to become an electrode which is easily Cu-electroplated (see Fig. 2a). After the Pt sputtering process is completed, Cu layer is deposited on the Pt-sputtered PAN nanofibers via electroplating. The Cu-plated fibers are then dried in nitrogen atmosphere, preventing oxidation of electroplated fibers.

For the MOF solution, zeolitic imidazolate framework-8 (ZIF-8), typical of the MOF class of materials [46,47], was synthesized by mixing 0.5 mmol of zinc acetate hexahydrate [$C_2H_{15}O_8Zn$, 232.5 g mol^{-1}, Sigma-Aldrich] and 2 mmol of 2-methyl imidazole (2MI) [$C_4H_6N_2$, 82.10 g mol^{-1}, Sigma-Aldrich] in 50 mL of methanol [CH_4O, 32.04 g mol^{-1}, Sigma-Aldrich]. Following that, ZIF-8 nanocrystals were formed over 10 min—a process identified by the color change in the mixed solution from clear to cloudy white [48,49].

The prepared Cu microfiber mats were immersed in the ZIF-8 solution at the room temperature of 25 °C for 1 h, during which MOF nanocrystals were uniformly deposited on the surface of Cu microfibers (see Fig. 2b). After 1 h, the as-fabricated MOF/Cu microfiber mats were washed using a clean methanol solution and then dried at room temperature for 24 h. Fig. 2b shows the changes in the diameter and morphology of fibers after Cu electroplating and MOF deposition. Here, the ZIF-8 nanocrystals could be strongly adhered to the Cu microfibers due to a chemical reaction. In other words, when the Cu microfibers were dipped into the zinc acetate hexahydrate/2MI solution (cf. Fig. 2a), Cu formed a Cu complex by the 2MI that existed in the MOF solution. Then, the Cu complex and Zn ions in the MOF solution were chemically linked to each other, thus facilitating a strong adhesion of ZIF-8 nanocrystals to the surface of Cu microfibers. On the other hand, the growth (or formation) of ZIF-8 nanocrystals after the adhesion is associated with the deprotonation of 2MI. The deprotonation of 2MI results in the imidazolium ions. Then, these imidazolium ions and the Zn^{2+} ions provided by dissolution of the Zn salt react with each other, forming six-membered rings by bridging N atom, which leads to the formation of ZIF-8 crystals with rhombohedral shape [50,51].

2.2. Characterization

The morphology of PAN nanofibers, Cu microfibers, and MOF/Cu microfibers was characterized using a high-resolution scanning electron microscope (HR-SEM, Philips Co., Netherlands) at the electron beam voltage of 15 kV. The average fiber diameter for each case was found by averaging the measured diameters of 50 fibers observed in each SEM image. This was done using the *I-measure*

software to measure the diameter of each fiber within an image. A field-emission scanning electron microscopy coupled with energy-dispersive X-ray spectroscopy (FE-SEM/EDS, Quanta 250 FEG, FEI) was also used to observe the surface morphologies and elements of the MOF/Cu microfibers.

To analyze the crystallinity of fibers, X-ray diffraction (XRD, D/max-2500, Rigaku, Japan) was employed under the following operating conditions: Cu Kα radiation over the diffraction angle (2θ) range of 10–80°. The Fourier-transform infrared (FTIR) spectroscopy was used to measure infrared absorption and emission spectra from fibers, where FTIR spectra in the 4000–400 cm^{-1} range were obtained using FTIR spectrometer (LabRam ARAMIS IR2, Horiba Jobin Yvon). The X-ray photoelectron spectroscopy (XPS, X-TOOL, ULVAC-PHI) was also employed to measure the elemental compositions at the fiber surfaces.

The PM filtration efficiency of fibrous filters was assessed using a house-made experimental setup. The efficiency was calculated based on the correlation between the amounts of PM in the input and after filtration, where an electronic scale (PAG214C, Ohaus, USA) was used to measure the PM mass. Details of the efficiency measurement method are discussed in Section 3.3.

To investigate the mechanical durability of PAN nanofibers, Cu microfibers, and MOF/Cu microfibers, tensile and puncture tests were conducted using a house-made mechanical tester comprising a force gauge (FG-6020SD, Lutron Electronic, USA) and a syringe pump (Legato 100, KD Scientific Inc., USA).

For the measurement of the pressure drop on the fibrous filters, a pressure gauge (DPG 3000, New-Flow Technologies, Inc., accuracy: ±0.5 % of full scale) was installed in the cylindrical experimental setup (cf. Fig. 3).

2.3. Corona discharge

To effectively capture PM delivered in air flow through the filter, an alternating-current (AC) corona discharge method was employed in the present study to negatively pre-charge PM [52]. Corona discharge can generate anions by creating the free electron avalanches in air. Here, the electrons are generated by a high-frequency air ionizer (Zapp II, Shishido Electrostatic, LTD., Japan) attached to the PM feeder (Fig. 3), thus, negatively charging the PM. For the PM, Cu powder (~625 mesh, average particle size of 0.50–1.5 μm, 99 % metal basis, Alfa Aesar) was used. Rhodamine B ($C_{28}H_{31}ClN_2O_3$, 479.01 g mol^{-1}, Sigma-Aldrich) powder was also used as a model PM, with which not only the filtration efficiency of fibrous filters with the Rhodamine B powder, but also the decomposition capacity of such filters toward Rhodamine B solution in DI water were investigated. To ensure comparable particle sizes for Rhodamine B and Cu powders, the Rhodamine B powder was pulverized using a mortar. After pulverization was performed, the size of the Rhodamine B powder particles, as confirmed by SEM, was about 1–3 μm in diameter (Fig. S1).

2.4. Filtration test

To demonstrate the filtration performance of the fibrous filters, an acrylic experimental setup sketched in Fig. 3 was used. It consisted of two parts: a PM feeder for supplying PMs attached to air ionizer and a cylindrical chamber for investigating the filtration performance. The fibrous filter and vacuum cleaner filter were installed inside the cylindrical chamber.

The PM feeder initially contained the electrically neutral Cu powder employed as a model PM in the present study. The inlet and outlet channels were installed for air-in and -out, respectively. First, ionized air from the ionizer (cf. Section 2.3) was supplied to the PM feeder through the inlet channel (Fig. 3a). As a result, the PM in the feeder was negatively charged (Fig. 3b) [21,53]. Finally, the negatively charged PM was directly supplied into the cylindrical chamber through the outlet channel of the PM feeder (Fig. 3c). Here, because the supplied PM in the chamber was negatively charged, the PM passing through the grounded MOF/Cu microfiber filter, was efficiently removed from the air flux by the Coulomb force (Fig. 3c). It should be emphasized that, without the PM pre-charging using the corona discharge ionizer (*i.e.*, filtering uncharged PM), the PM could only be filtered via the standard filtration mechanisms: the inertial interception, diffusion, or with the help of 50 nm fibers embedded in the filter, by the van der Waals forces [54].

3. Results and discussion

3.1. Morphologies and physicochemical properties of PAN nanofibers, Cu microfibers, and MOF/Cu microfibers

Fig. 4a–c show the SEM images of electrospun PAN nanofibers, Cu-electroplated microfibers, and MOF/Cu microfibers (cf. Experimental section). As revealed in the SEM images, each case exhibits different fiber diameters and morphologies. The average diameters of the PAN nanofibers, Cu microfibers, and MOF/Cu microfibers are 0.50 ± 0.02, 2.30 ± 0.10, and 2.30 ± 0.16 μm, respectively. It should be emphasized that the Cu electroplating time during fabrication of the MOF/Cu microfibers is intentionally reduced by half, compared to that for the Cu microfibers to yield the MOF/Cu microfibers with diameters similar to those of Cu microfibers. The sub-micrometer PAN fibers yield microscale fibers upon Cu plating (Fig. 4b). Interestingly, MOF crystals grow on the surfaces of the Cu microfibers as rhombic dodecahedra with approximate dimensions of 200 nm × 200 nm × 200 nm for each crystal (Fig. 4c).

Photographs of different filters based on PAN nanofibers, Cu microfibers, and MOF/Cu microfibers are shown in the second row of Figs. 4a–c, respectively. After the Cu electroplating was performed, not only did PAN nanofibers turn brown in color, but the fiber mat also became slightly stiffer than the original PAN nanofiber mat. The stiffness of the MOF/Cu microfiber mat is similar to that of the Cu microfiber mat, while the color is slightly darker. As shown in Fig. 4d, each MOF (or ZIF-8) crystal initially has a size of less than 100 nm at the MOF deposition time of 10 min. However, the crystal size increases as the deposition time is increased (Fig. 4e and f). The MOF crystals are in the form of truncated rhombic dodecahedra [55], consistent with previously reported methanol-based ZIF-8 crystals [50,56]. The result of elemental mapping of the MOF/Cu microfiber is presented in Fig. S2. The elemental mapping images of Cu, Zn, and C (carbon) on the MOF/Cu microfiber were clearly observed. Note that the presence of C outside the microfiber was due to the carbon tape used for fixing the fiber.

During the fabrication process, porosity of the fibrous filters was controlled to provide comparable filtration efficiency, affected only by the different materials used. As a result, equivalent porosities of 0.28 were achieved in the different fibrous filters. The cross-sectional porosity was evaluated based on the analysis of the SEM images. The topmost fiber layer in each SEM image was isolated and converted into color fiber and white pore domains (cf. Fig. 4g–i). Subsequently, Image J software was used to evaluate the porosity as the ratio of the number of white pixels (open space) to the total number of pixels in the image. Three SEM images were used for each filter type, and the average values of the porosities were used in each case.

Fig. 5a shows the XRD pattern of the MOF/Cu microfibers. Diffraction peaks are observed at the 2θ values of 43.4°, 50.5°, and 74.1°, corresponding to the (111), (200), and (220) planes of Cu, respectively. These diffraction peaks are characteristic of face-centered cubic (FCC) Cu [57]. Note that no peaks indicating impurities (*i.e.*, CuO and Cu_2O) are observed in the MOF/Cu

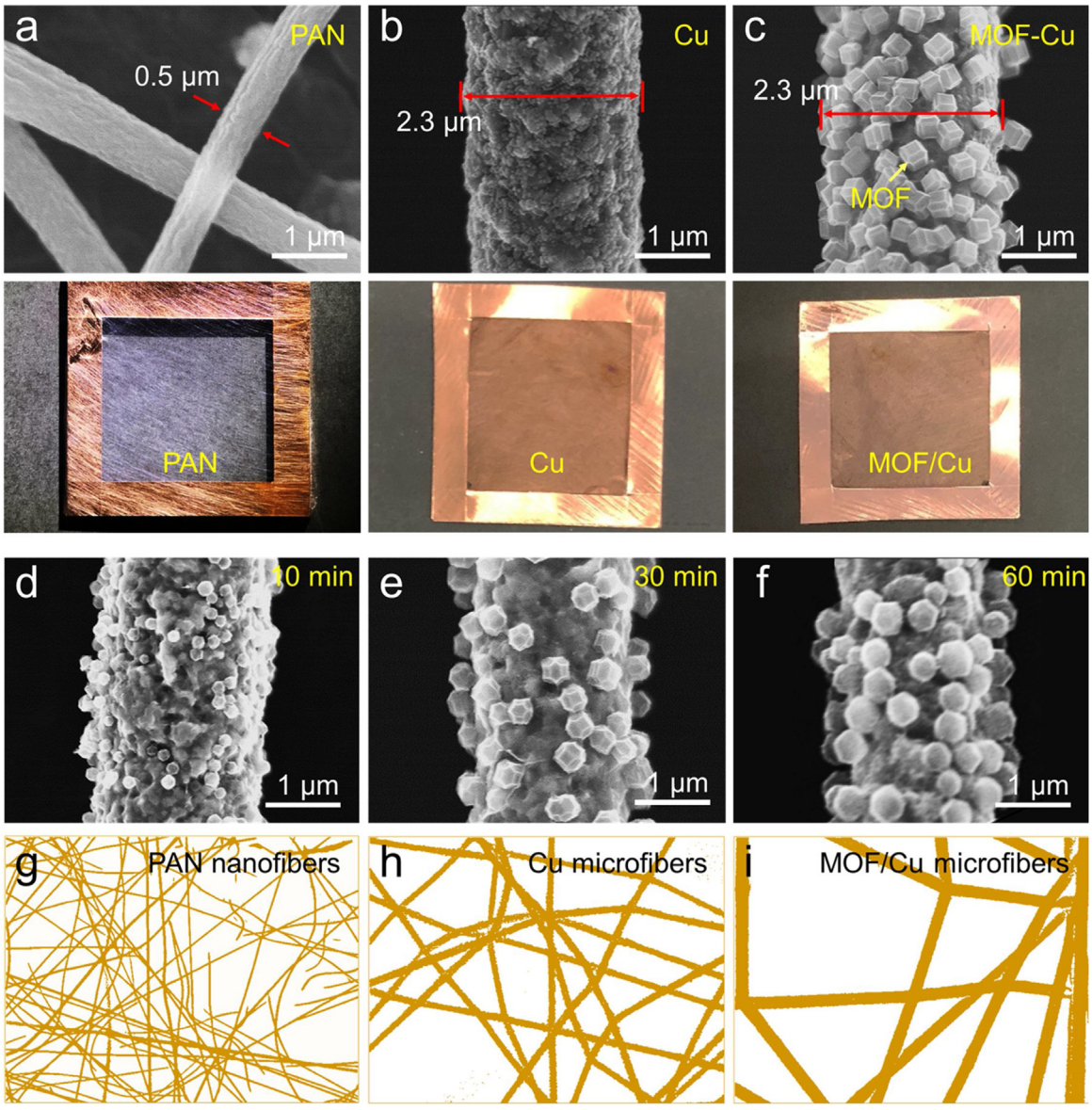

Fig. 4. SEM images and the corresponding photographs of different fibrous filters based on: (a) PAN nanofibers, (b) Cu microfibers, and (c) MOF/Cu microfibers. SEM images of individual MOF/Cu microfibers with varying MOF deposition times of: (d) 10 min, (e) 30 min, and (f) 60 min. Processed images of (g) PAN nanofibers, (h) Cu microfibers, and (i) MOF/Cu microfibers.

microfibers. Fig. 5b shows the magnified XRD pattern of the MOF/Cu microfibers in the 2θ range of 10°–20°. Notable peaks are observed at 2θ = 12.7°, 14.7°, 16.4°, and 18.0° and attributed to the (112), (022), (013), and (222) planes of ZIF-8, respectively. These diffraction peaks observed with the MOF/Cu microfibers agree well with the previously reported sodalite structure of typical ZIF-8 [58–61].

The FTIR result in Fig. 5c describes the chemical substances and structures of ZIF-8 present at the surfaces of the MOF/Cu microfibers. Bands related to ZIF-8 are observed at 3455, 3135, 2928, 1635, 1585, 1458, 1425, 1385, 1309, 1146, 995, 760, and 694 cm^{-1}, consistent with those previously reported [62–64]. In detail, the band at 3455 cm^{-1} is attributed to the NH— stretching vibration and the OH stretching vibration of water. The small bands at 3135 and 2929 cm^{-1} indicate aromatic and aliphatic CH— asymmetric stretching vibrations, respectively. The C=C stretching mode is revealed at 1635 cm^{-1}, and the peak at 1585 cm^{-1} represents C=N stretching vibrations. The bands at 1309–1458 cm^{-1} are attributed to full ring stretching, and the peak at 1146 cm^{-1} arises from the aromatic CN— stretching mode. The peaks at 995 and 760 cm^{-1} relate to the C—N and CH— bending modes, respectively. The peak at 694 cm^{-1} corresponds to the ring out-of-plane bending vibration [58,62–64].

Fig. 5d–f show the XPS results indicating the presences of C, Cu, and Zn, which is consistent with the result of the elemental mapping in Fig. S2. The C 1*s* peak in Fig. 5d corresponding to the MOF/Cu microfibers appears at the binding energy of 283.8 eV, where C 1*s* peaks below 284 eV indicate carbon existing in the sp^2 state [65,66]. The Cu 2*p* spectrum in Fig. 5e reveals two dominant peaks at 933.3 and 953.2 eV, assigned to the Cu $2p_{1/2}$ and Cu $2p_{3/2}$ orbitals of CuO, respectively. Two satellite peaks, demonstrating the presence of divalent Cu rather than Cu(0), are also observed in Fig. 5e [67,68]. The peak at the binding energy of 1021.8 eV in Fig. 5f corresponds to Zn $2p_{3/2}$, while the other one at 1044.8 eV is attributed to Zn $2p_{1/2}$. The binding energy distance between these two peaks is 23.0 eV, indicating that Zn ions in the composites are divalent cations [68,69].

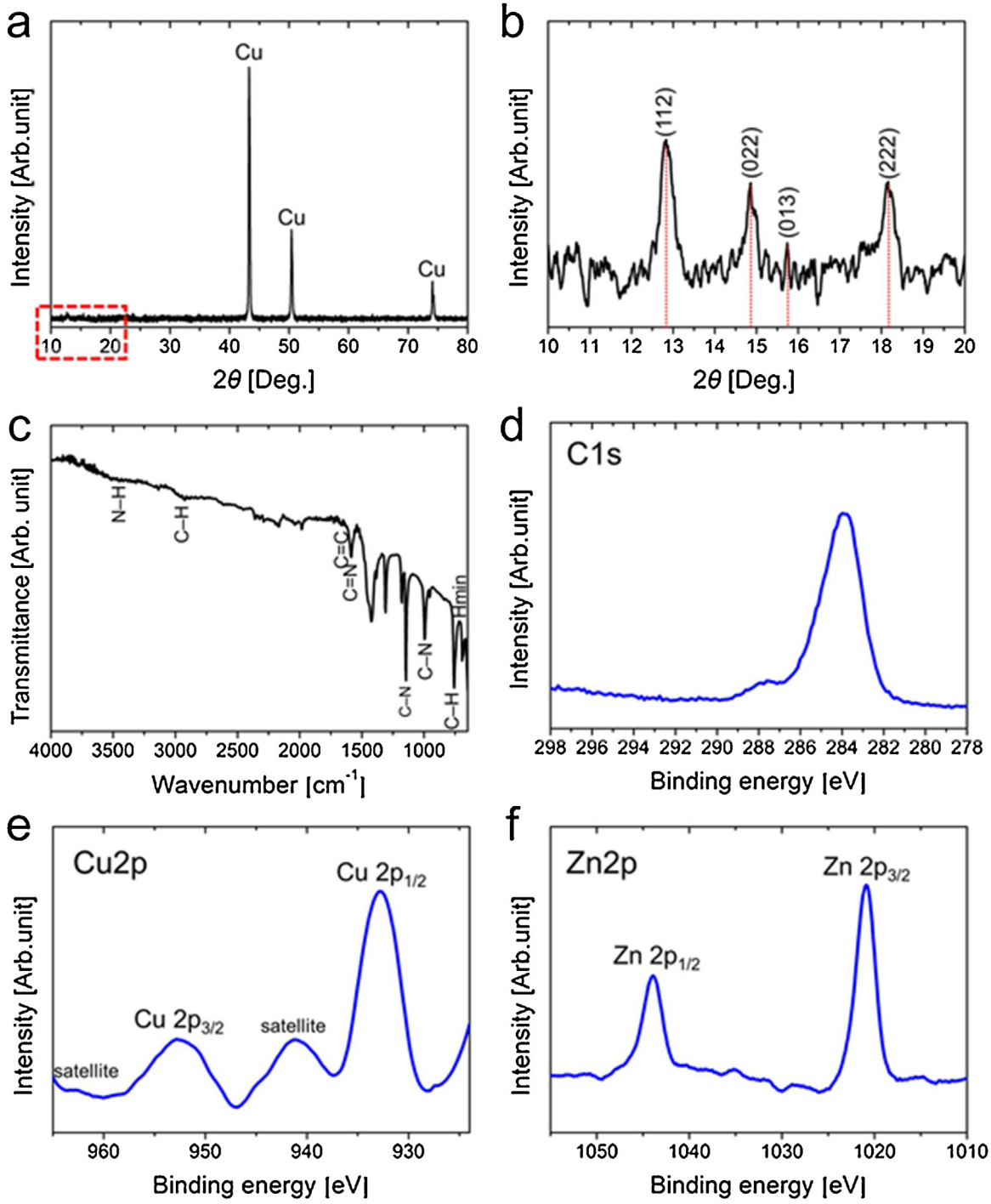

Fig. 5. XRD patterns of MOF/Cu microfibers in (a) broad and (b) narrow ranges. (c) FTIR spectrum of MOF/Cu microfibers. High-resolution XPS spectra of MOF/Cu microfibers for (d) C 1*s*, (e) Cu 2*p*, and (f) Zn 2*p* energy levels.

3.2. Mechanical properties of PAN nanofibers, Cu microfibers, and MOF/Cu microfibers

Fig. 6 illustrates the mechanical behavior of the PAN nanofibers, Cu microfibers, and MOF/Cu microfibers. For the mechanical tests (see Fig. 6a), each fiber mat was cut into small 2.0 cm × 2.5 cm rectangles. For the tensile test, a cut-off specimen was clamped between the grips of the syringe pump, and the force gauge measured the load (or stress) applied by the pump during the tensile test. The initial distance between the grips of the pump was 2 cm, and the strain rate in the tests was 0.05 mm s^{-1}. For the puncture test (see. Fig. 6b), a cut-off specimen was tightly fixed by the grips of the pump to prevent folding during the puncture test. A 7-mm-diameter tip was used to puncture the specimen in the out-of-plane direction. The tip speed was 0.05 mm s^{-1}. The results of the tensile and puncture tests for different fibrous filters are described in Fig. 6c and d, respectively. To minimize the differences in other properties (*i.e.*, porosity) between different fibrous filters, the mats were deliberately fabricated with similar porosity (cf. Section 3.1). For this reason, it should be emphasized that the PAN nanofibers were prepared with the electrospinning time of 180 s, three times

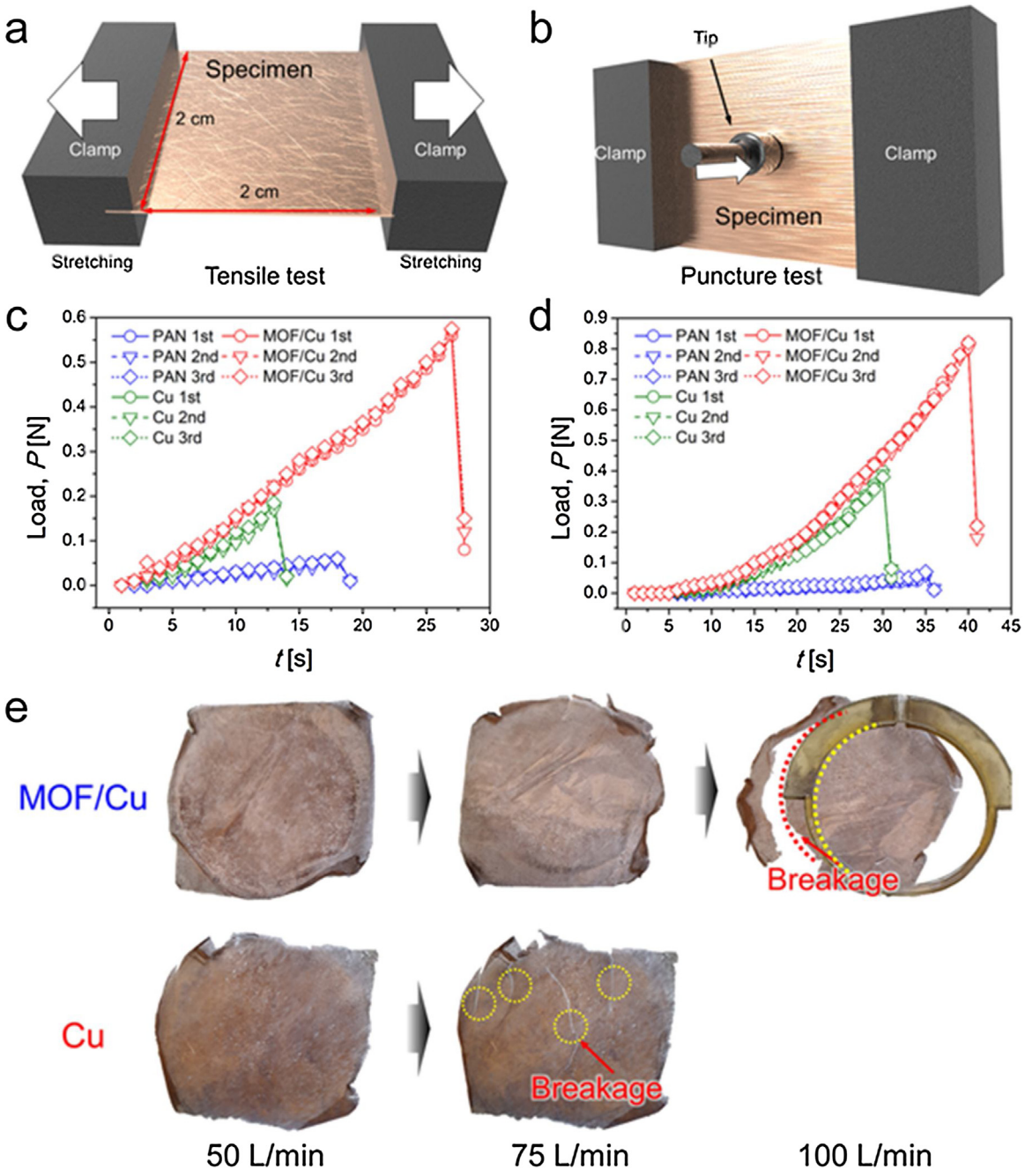

Fig. 6. Schematics of (a) tensile and (b) puncture tests. Results of mechanical tests for different fiber mats: (c) tensile test and (d) puncture test. (e) Photographs of MOF/Cu microfiber mat and Cu microfiber mat after air flow tests.

longer than the time taken for preparing the corresponding PAN nanofibers used to form Cu and MOF/Cu microfibers (60 s).

Figs. 6c and d show the results of three tests per filter type in the cases of the tensile and puncture tests, respectively. In the tensile test (Fig. 6c), the load (or stress) is applied from t = 1 s and gradually increased over time. For the PAN nanofiber mat, as the load reaches 0.06 N (t = 18 s), the PAN nanofiber mat tears. In the case of the Cu microfiber mat, the slope of the load-vs-time line is higher than that for the PAN nanofiber mat; the mat is torn when the load reaches 0.18 N (t = 13 s), indicating that the mat stiffness is significantly increased because of Cu electroplating. The stiffness of the MOF/Cu microfiber mat is similar to that of the Cu microfiber mat. However, unlike the Cu microfiber mat that tears at 0.18 N, the MOF/Cu microfiber mat withstands loads up to 0.56 N, three times higher than the one withstood by the Cu microfiber mat. That is, the tensile tests demonstrate that the Cu electroplating and MOF deposition have positive effects on the stiffness and stretchability of fiber filters.

Fig. 6d shows the results of the puncture tests for different fiber mats. In these tests, a 5-mm-diameter tip is used to push the center of the fiber mat in the out-of-plane direction at a speed of 0.05 mm s^{-1} (cf. Experimental section). Similar trends as in the tensile tests are observed in the puncture tests. For the PAN nanofiber mat, although the magnitude of load increase is small, the load value tends to gradually increase over time up to the maximum of 0.06 N at t = 35 s. In the case of the Cu microfiber mat, the load increases sharply, and the maximum load is 0.4 N at t = 30 s, when the fiber mat is torn. Similarly, to the tensile tests, the puncture test reveals

that stiffness of fiber mat is enhanced after Cu electroplating. For the MOF/Cu microfiber mat, the slope of the load-vs-time line is similar to that of the Cu microfiber mat; however, the maximum load is increased up to 0.84 N. That is, regardless of the similar average diameters of the Cu and MOF/Cu microfibers (see Fig. 4), the maximum load revealed by the MOF/Cu microfiber mat is twice that of the Cu microfiber mat, demonstrating the superior mechanical durability of the MOF/Cu microfiber filter compared to the bare Cu microfiber filter.

The excellent mechanical properties observed in the puncture tests are reconfirmed in the air flow tests. In these tests, the flow rate of air passing the fiber filter was varied to determine the maximum achievable flow rate for the fibrous filter performance (cf. Fig. 3c). The fibrous filter was installed inside a cylindrical chamber as described in Fig. 3c, and the flow rate of air passing the fibrous filter was increased from 50 to 75 and 100 L min^{-1} to assess its practical durability in the air flow. Since the flow rate of air passing through the filter was constant, the corresponding average velocity of air can be obtained as $V = QA^{-1}$, where V is the velocity of air flow, Q is the flow rate, and A is the cross-sectional area of the cylindrical setup (cf. Fig. 3). The values of velocity for the flow rates of 50, 75, and 100 L min^{-1}, were 42.5, 63.7, 84.9 cm s^{-1}, respectively.

At the air velocity of 42.5 cm s^{-1}, neither the Cu nor the MOF/Cu microfiber mat is torn (Fig. 6e). However, as the velocity is increased to 63.7 cm s^{-1}, the Cu microfiber mat was damaged (Fig. 6e); it could not be reused thereafter because of this damage. The MOF/Cu microfiber mat remained durable at the velocity of 63.7 cm s^{-1}, but began to crack as the velocity reached 84.9 cm s^{-1} (Fig. 6e). However, unlike the Cu microfiber mat in which breakage occurred centrally, the MOF/Cu microfiber mat underwent breakage at the points of contact with the fixing bracket. This result shows that the mechanical durability of the MOF/Cu microfiber mat against the normal stress is superior to that of the Cu microfiber filter, as observed in the puncture tests depicted in Fig. 6c and d.

3.3. Filtration efficiency and reusability of MOF/Cu microfiber filter

Fig. 7a and b describe the filtration performance of different MOF/Cu microfiber filters against PM (Cu powder). Five filtration tests were performed with each type of the filter, and the calculated average efficiency values are plotted in the bar chart in Fig. 7a. The filtration efficiency η is defined using of the amount of PM supplied to the cylindrical chamber (cf. Fig. 3c) and the one filtered by the fibrous filter in 180 s (cf. Fig. 3c):

$$\eta = (1 - \frac{M_v}{M_0}) \times 100\% = \frac{M_f}{M_0} \times 100\% \quad (1)$$

where, M_0, M_v, and M_f are the average values of the mass of PM supplied to the chamber, filtered by the vacuum cleaner filter, and filtered by the fibrous filter, respectively.

Fig. 7a shows the filtration efficiency of the MOF/Cu microfiber filters with and without the ionizer and at different MOF deposition times. Color and black bars represent cases employing and not employing the ionizer, respectively. At the MOF deposition time of 0 min, the pristine Cu microfiber mat without MOF deposition is used. It should be emphasized that the Cu electroplating times in each case in Fig. 7a are adjusted to yield similar fiber diameters in different cases. That is, for the MOF deposition times of 0, 10, 30, and 60 min, the corresponding Cu electroplating times were 60, 50, 40, and 30 s, respectively.

When the ionizer is not used, all the MOF/Cu microfiber filters exhibited low filtration efficiencies of ~24 %. By contrast, when the ionizer was used, the filtration efficiency in all cases was about 90 % regardless of the MOF deposition time; the efficiency is gradually increased with increasing MOF deposition time. Interestingly, regardless of the fact that MOF/Cu microfibers with long MOF deposition times (*i.e.*, 30 and 60 min) have shorter Cu electroplating times than the MOF/Cu microfibers with short MOF deposition times (*i.e.*, 0 or 10 min), significant difference in filtration efficiency is not observed, despite the varying amounts of Cu-plating. Thus, this result indicates that electrostatic filtration is mainly associated with volume charges rather than surface electrical resistivity.

On the other hand, the use of multiple layers in the fibrous filter could result in the improvement of the filtration efficiency. Fig. 7b describes the results related to the filtration efficiency with increasing the number of layers of the MOF/Cu microfiber filters (N_{layer}). Note that a single layer of the MOF/Cu microfiber filter was fabricated with the electroplating time of 30 s and the MOF deposition time of 60 min. When the value of N_{layer} was 3, the corresponding efficiencies were 25.3 % with the ionizer off and 94.0 % with the ionizer on. As the value of N_{layer} increased to 5, the efficiencies also increased to 26.7 % with the ionizer off and 97.9 % with the ionizer on. Although the efficiency could be enhanced with increasing the value of N_{layer}, the pressure drop also slightly increased from 0 to 207 Pa due to an increase in thickness of the overall filter structure, as described in Figs. 7c and d.

Fig. 7e describes the result of the cycling test involving the MOF/Cu microfiber filter (N_{layer} = 1); herein, the MOF/Cu microfiber filter fabricated under the MOF deposition time of 60 min is tested. The filtration efficiency is assessed at each time in 3 min of operation with the ionizer on and in 3 min with the ionizer off. Note that the fibrous filter was cleaned after each 6-min cycle (cf. one cycle included 3 min with the ionizer on and 3 min without the ionizer) using air blowing. This cleaning was performed using a 3 mm in diameter nozzle blowing air at the rate of 50 mL s^{-1} [16]. This cycle was repeated 20 times. As described in Fig. 7e, the maximum filtration efficiency reaches 92 % when the ionizer is turned on, whereas the efficiency without the ionizer is only 20–30 %. There is a slight variation in the filtration efficiency between 20 and 30 % when the ionizer is off, while a nearly constant filtration efficiency value of about 92 % is found when the ionizer is on.

Fig. 7f illustrates the change in the filtration efficiency of the MOF/Cu microfiber filter with the ionizer on over 50 cycles, wherein each cycle includes both filtration and cleaning stages. The average filtration efficiency over 50 cycles is 91 %. The efficiencies at N = 1, 2, and 27 are 93 %, 91 %, and 91 %, respectively. During the cycles from N = 28–50, the efficiency is slightly decreased to 90 %. As observed in Fig. 7g, some PM remains in the filter even after the cleaning stage as the number of cycles exceeds N = 25, which causes small fluctuations and a slight decrease in the efficiency during the recycling test, as observed in Fig. 7f. Fig. S3 illustrates the change in the filtration efficiency for 150 cycles. The average filtration efficiency over 150 cycles was 90 %. The efficiencies at N = 100 and 150 were 89 % and 87 %, respectively.

Figs. 7h–j describe the SEM images of the MOF/Cu microfiber filter before and after filtration, and after cleaning. Here, the MOF/Cu microfiber filter with the MOF deposition time of 60 min was used and the ionizer was on for 3 min. In addition, filtration and cleaning were repeated 50 times. Fig. 7h corresponds to the SEM image of the MOF/Cu microfiber filter before filtration (cf. Fig. 4), while Fig. 7i shows the filter after one filtration cycle (*i.e.*, N = 1), in which the PMs (Cu particles) were not only clustered at the MOF/Cu microfibers, but also stuck between the microfibers. On the other hand, Fig. 7j shows the SEM image of the MOF/Cu microfiber filter after cleaning, where the filter was cleaned after 50 cycles (cf. Fig. 7f). It is clearly seen that the PMs could be effectively removed after cleaning, regardless of multiple cycles of N = 50. In addition, the MOFs on the microfibers were not detached at all even after cleaning due to the strong adhesion of MOF to the Cu microfibers.

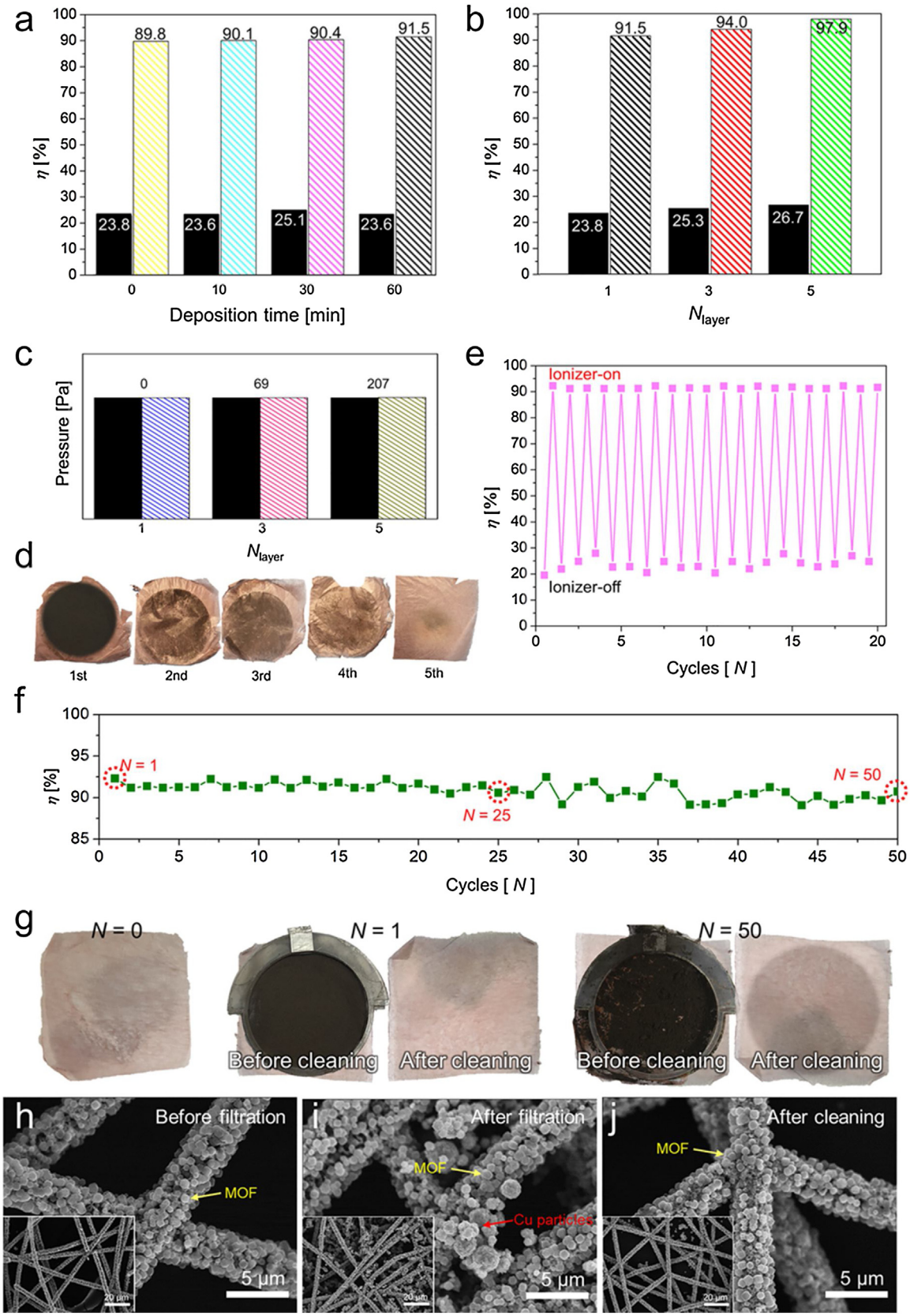

Fig. 7. Comparison of the filtration efficiency (a) of different MOF/Cu microfiber filters against Cu powder illustrating the effect of the pre-ionization use and MOF deposition time, and (b) with using different number of layers of the MOF/Cu microfiber filter. (c) Results for air pressure before (black column) and after (diagonal-lined column) passing the filter with varying the number of layers of the MOF/Cu microfibers. (d) The corresponding snapshots of each layer at N_{layer} = 5 after the PM filtration (where the 1 st layer was placed at the side where PMs entered the filter). Results of the cycling tests of the MOF/Cu microfiber filters for (e) 20 cycles with the ionizer on and off and (f) 50 cycles with the ionizer on. (g) Photographs of the MOF/Cu microfiber filter before the filtration test (N = 0) and after the filtration test of 1 cycle (N = 1) and 50 cycles (N = 50). SEM images of the MOF/Cu microfiber filter (h) before filtration (N = 1), (i) after filtration (N = 1), and (j) after cleaning (N = 50).

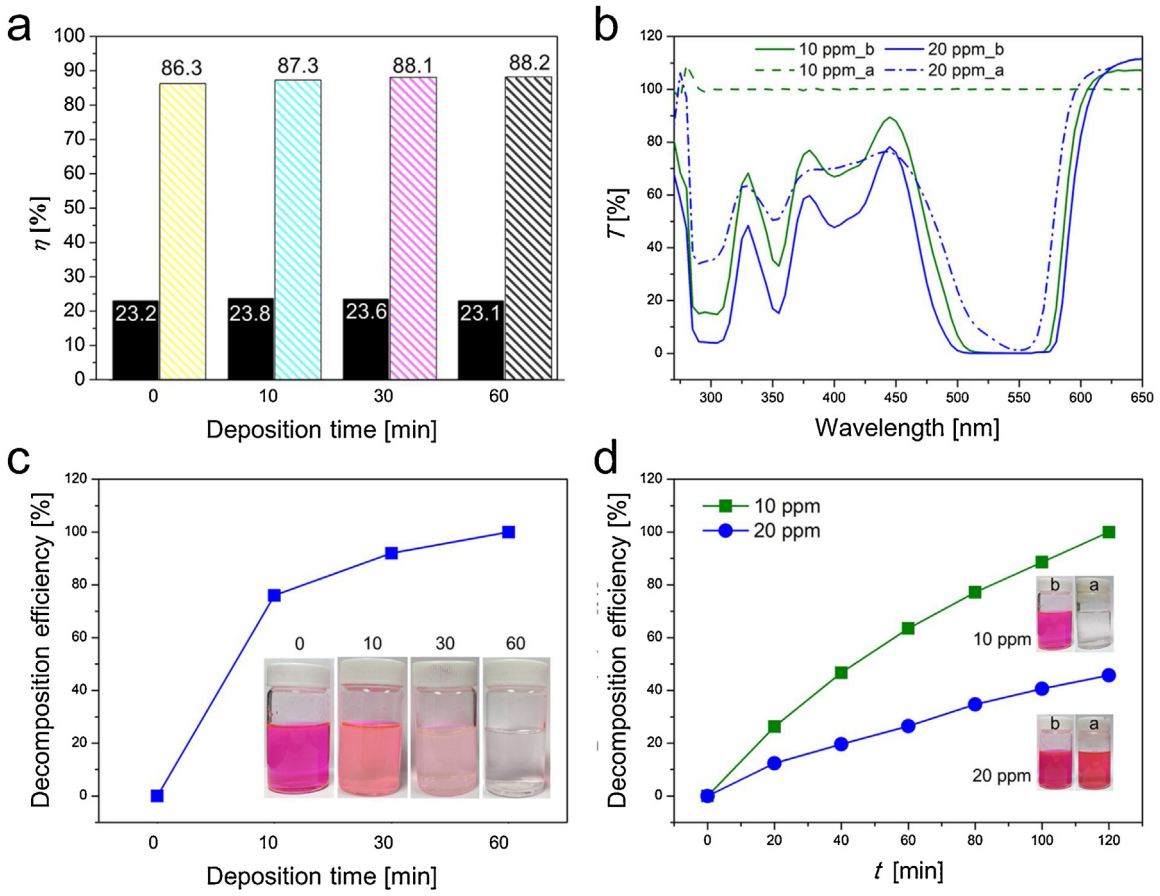

Fig. 8. (a) Comparison of filtration efficiency of different MOF/Cu microfiber filters against Rhodamine B powder with and without ionization at different MOF deposition times. (b) Transmittance spectra of Rhodamine B solution before (denoted as b) and after UV irradiation with MOF/Cu microfiber filter (denoted as a). The decomposition efficiency of MOF/Cu microfiber filters (c) at different MOF deposition times and (d) as a function of UV irradiation time.

Table 2
Comparison of nanofiber-based filters.

Particle diameter [nm]	Filtration efficiency [%]	Filter thickness [μm]	Face velocity [m s^{-1}]	Pressure loss [Pa]	Duration time [min]	Ref.
2500	99	1.25	0.05	–	–	[76]
2500	99	53.8	0.053	123.97	–	[77]
300	100	0.4	0.05	73.5	–	[78]
300	99	1700	0.05	68	–	[79]
300	100	150	2.2	521	36	[80]
100	98	20	0.05	85	60	[81]
< 1500	**92 (1 layer) 94 (3 layer) 98 (5 layer)**	**4 12 20**	**42.5**	**0 69 207**	**900**	**This study**

3.4. Rhodamine B-tested decomposition capacity of MOF/Cu microfiber filter

The use of MOF deposited on the Cu microfibers enables the improvement of the filtration efficiency from 89.9%–91.5% (cf. Section 3.3) and enhancement of mechanical durability (cf. Sections 3.2). In addition, accounting for the fact that MOFs, particularly ZIF-8, can decompose Rhodamine B, which is a known toxic chemical widely employed in the dye industry despite its carcinogenic properties [70,71], the Rhodamine B decomposing capacity of the MOF/Cu microfiber filter was also investigated in the present study.

First, the filtration efficiency of the MOF/Cu microfiber filter with the powder form of Rhodamine B was explored similarly to that of Cu powder (cf. Section 3.3). The corresponding filtration tests with Rhodamine B were conducted under visible light conditions. Although the adsorption efficiency of MOF for Rhodamine B can be enhanced under the UV light conditions because the UV has a sufficient energy to excite the electrons in the valence band to the conduction band [72], the filtration tests in this study were performed under the visible light conditions having in mind potential uses in various applications.

As shown in Fig. 8a, similarly to the results obtained with Cu powder, the overall filtration efficiency of MOF/Cu microfiber filters with pre-ionization is high in all cases. The efficiency value gradually increased from 86.3%–88.2% as the MOF deposition time increased from 0 to 60 min (cf. Section 3.3).

On the other hand, compared to the filtration efficiencies exhibited by Cu powder with the ionizer on (cf. Fig. 7a), those revealed in the case of Rhodamine B powder were slightly lower by about 2–3 % (cf. Fig. 8a). In other words, although the size of Rhodamine B pow-

der was larger than that of Cu powder, the corresponding filtration efficiencies of Rhodamine B powder were lower than those for the Cu powder. This is attributed to the fact that Cu possesses a high (metallic) electrical conductivity, whereas Rhodamine B possesses a low electrical conductivity characteristic of dielectric materials [72,73], which facilitates a more significant charging of Cu powder compared to Rhodamine B, and thus, a more effective removal of Cu when using the ionizer.

Second, the decomposition capacity of the MOF/Cu microfiber filter was explored by immersing the fibrous filter into Rhodamine B aqueous solution. The MOF can decompose Rhodamine B dispersed in an aqueous solution under the UV light according to the following three steps (cf. Fig. S4) [72]: (i) The UV light causes the electrons in the valence band of Rhodamine B to jump out to the conduction band (where the energy bandgap is 2.87 eV) (cf. Fig. S4a). Then, the excited electrons are transferred to the Cu microfiber while the Rhodamine B is simultaneously converted into radical cation. (ii) The UV light also excites electrons in the valence band of MOF (ZIF-8, energy bandgap =5.5 eV) to its conduction band. Then, these electrons participate in production of oxygen radicals such as $O_2^{\bullet -}$, $O^{\bullet}OH$, and $^{\bullet}OH$ (Fig. S4b). (iii) The Rhodamine B radical cations then begin to react with the oxygen radicals, thus leading to the formation of degradation products (cf. Fig. S4c) [74].

Different concentrations of Rhodamine B solutions (*i.e.*, 10- and 20-ppm) were prepared and tested to investigate the decomposition capacity of the MOF/Cu microfiber filters (cf. Fig. 8b). In these experiments ionizer was not used with the MOF/Cu microfiber filter. The MOF/Cu microfiber filter fabricated at the MOF deposition time of 60 min was immersed in one of the solutions, following which the solution was irradiated with UV light for 2 h. Next, the fibrous filter was removed from the solution, and the corresponding transmittance values of the solutions were measured and compared with those recorded before UV irradiation. In both cases with the 10- and 20-ppm solutions, the transmittances were improved, indicating that the MOF/Cu microfiber filter effectively decomposes Rhodamine B dissolved in DI water. In particular, for the 10-ppm case, the transmittance of the Rhodamine B solution after the test was significantly improved, indicating the complete (because the transmittance was 100 %) decomposition of Rhodamine B.

Fig. 8c describes the change in the decomposition efficiency as a function of the MOF deposition time, when using different MOF/Cu microfiber filters. The 0-min case (corresponding to the bare Cu microfiber filter) reveals no decomposition of Rhodamine B. However, as the MOF deposition time is increased, the decomposition efficiency is significantly increased. For the MOF deposition time of 10 min, the 76 % efficiency is observed, and the efficiency approaches 100 % for the MOF deposition time of 60 min. The decomposition efficiency is defined as:

$$\delta = \frac{(100 - T_b) - (100 - T_a)}{(100 - T_b)} \times 100\% = \frac{T_a - T_b}{100 - T_b} \times 100\%, \quad (2)$$

where T_b is the transmittance value of the solution before UV irradiation, and T_a is the transmittance value after UV irradiation in the presence of MOF/Cu microfiber filter.

The decomposition efficiency over time is described in Fig. 8d; the transmittance of each solution is checked every 20 min. The low-concentration solutions of 10 and 20 ppm reveal gradual increase in the efficiency over time, with the final efficiencies of 100 % and 45.75 % obtained after 2 h, respectively. On the other hand, the degradation rate of Rhodamine B (k) can be obtained from the following pseudo-first order equation of Lagergren [75]:

$$\log(q_m - q_t) = \log(q_m) - \frac{kt}{2.303} \quad (3)$$

where q_t and q_m are the adsorbed amounts (mg g^{-1}) of Rhodamine B at time t (min) and at the equilibrium state (where the time was 120 min), respectively. The values of k for the MOF/Cu microfiber filter were 0.02 and 0.005 in the 10 and 20 ppm cases, respectively. They indicate that the efficiency of Rhodamine B degradation with the MOF/Cu microfiber filter was higher at the low concentration of Rhodamine B.

The filtration performance of the MOF/Cu microfiber filter was compared with those of the previously reported studies, as listed in Table 2. Although the filtration efficiency of a single layer of the MOF/Cu microfiber filter is lower than the others (see Table 2), that of the multi-layered MOF/Cu microfiber filter is comparable to the others. In addition, it should be emphasized that the multi-layered MOF/Cu microfiber filter still has the small thicknesses of < 20 μm. Note also that, the filters developed here exhibited high filtration efficiencies in spite of the high velocity of the air flow (42.5 m/s) that is 1–3 orders faster than the velocities performed in the other studies. Furthermore, the MOF/Cu microfiber filters also revealed lower values of the pressure loss compared to those in several other studies.

4. Conclusion

In this study, high-performance, reusable, and mechanically durable electrostatic air filters were developed, and their filtration performance was investigated. The air filters mainly comprised of nonwoven metallized microfibers were formed using electrospinning and electroplating. Metal-organic-framework (MOF) nanocrystals were additionally grown on the surface of these metallized microfibers. The MOF nanocrystals on the surface of metalized microfibers were physicochemically adhered, facilitating strong adhesion even after multiple filtrations. In particular, the decoration of nanoscale MOF crystals on the surface of the Cu microfibers enabled significant improvements in the mechanical durability of the resulting fibrous filters (~150 cycle), along with enhancement in the filtration efficiency (~98 %). In addition, the use of MOF in the fibrous filters facilitated decomposition of toxic chemicals such as Rhodamine B under UV irradiation, when it was rinsed from the filter. Because the hybrid electrostatic air filters developed in this study not only demonstrated an outstanding filtration efficiency but also a remarkable reusability, they hold great promise as commercially viable and high-performance electrostatic air filters.

Declaration of Competing Interest

The authors declare that they have no known competing financial interests or personal relationships that could have appeared to influence the work reported in this paper.

Acknowledgements

This work was supported by The National Research Foundation of Korea (NRF) grant funded by the Korea government (MSIT)(No. NRF-2020R1A5A1018153). The authors acknowledge King Saud University, Riyadh, Saudi Arabia, for funding this work through Researchers Supporting Project number (RSP-2020/30).

Appendix A. Supplementary data

Supplementary material related to this article can be found, in the online version, at doi:https://doi.org/10.1016/j.jmst.2020.12.065.

References

[1] M. Andreae, D. Rosenfeld, Earth. Rev. 89 (2008) 13–41.
[2] N. Mahowald, Science 334 (2011) 794–796.

[3] R. Zhang, J. Jing, J. Tao, S.-C. Hsu, G. Wang, J. Cao, C.S.L. Lee, L. Zhu, Z. Chen, Y. Zhao, Atmos. Chem. Phys. 13 (2013) 7053–7074.
[4] D.E. Horton, C.B. Skinner, D. Singh, N.S. Diffenbaugh, Nat. Clim. Chang. 4 (2014) 698–704.
[5] C. Liu, P.-C. Hsu, H.-W. Lee, M. Ye, G. Zheng, N. Liu, W. Li, Y. Cui, Nat. Commun. 6 (2015) 6205.
[6] K.-H. Kim, E. Kabir, S. Kabir, Environ. Int. 74 (2015) 136–143.
[7] J. Zhao, Q. Zhao, C. Wang, B. Guo, C.B. Park, G. Wang, Mater. Des. 131 (2017) 1–11.
[8] S.-J. Cao, D. Cen, W. Zhang, Z. Feng, Build. Environ. 126 (2017) 195–206.
[9] S.-J. Cao, C. Ren, Build. Environ. 144 (2018) 316–333.
[10] Y. Bai, C.B. Han, C. He, G.Q. Gu, J.H. Nie, J.J. Shao, T.X. Xiao, C.R. Deng, Z.L. Wang,Adv. Funct. Mater. 28 (2018), 1706680.
[11] M. Brauer, M. Amann, R.T. Burnett, A. Cohen, F. Dentener, M. Ezzati, S.B. Henderson, M. Krzyzanowski, R.V. Martin, R. Van Dingenen, Environ. Sci. Technol. 46 (2012) 652–660.
[12] J.H. Park, K.Y. Yoon, J. Hwang, Build. Environ. 46 (2011) 1699–1708.
[13] B. Shi, L. Ekberg, Environ. Sci. Technol. 49 (2015) 6891–6898.
[14] Z. Feng, Z. Long, T. Yu, J. Electrostat. 83 (2016) 52–62.
[15] E. Tian, J. Mo, Energy Build. 186 (2019) 276–283.
[16] M.-W. Kim, S. An, H. Seok, S.S. Yoon, A.L. Yarin, ACS Appl. Mater. Interfaces 11 (2019) 26323–26332.
[17] L. Wang, Y. Wu, G. Li, H. Xu, J. Gao, Q. Zhang,Chem. Eng. J. (2020), 125755.
[18] B. Shi, ASHRAE Trans. 118 (2012) 602–611.
[19] S. Wang, X. Zhao, X. Yin, J. Yu, B. Ding, ACS Appl. Mater. Interfaces 8 (2016) 23985–23994.
[20] M.H. Kim, W.J. Lee, D.H. Lee, S.W. Ko, T.I. Hwang, J.W. Kim, C.H. Park, C.S. Kim, J. Nanosci. Nanotechnol. 18 (2018) 2132–2136.
[21] K.R. Parker, Applied Electrostatic Precipitation, Springer, Dordrecht, 1997.
[22] H.-J. Kim, B. Han, Y.-J. Kim, S.-J. Yoa, J. Aerosol Sci. 41 (2010) 987–997.
[23] Z. Li, Y. Liu, Y. Xing, T.-M.-P. Tran, T.-C. Le, C.-J. Tsai, Environ. Sci. Technol. 49 (2015) 8683–8690.
[24] M. Gao, Y. Zhu, X. Yao, J. Shi, W. Shangguan, Powder Technol. 348 (2019) 13–23.
[25] R. Thakur, D. Das, A. Das, Sep. Purif. Rev. 42 (2013) 87–129.
[26] J.H. Park, K.Y. Yoon, K.C. Noh, J.H. Byeon, J. Hwang, J. Aerosol Sci. 41 (2010) 935–943.
[27] M.W. Lee, S. An, K.Y. Song, B.N. Joshi, H.S. Jo, S.S. Al-Deyab, S.S. Yoon, A.L. Yarin,J. Appl. Phys. 118 (2015), 245307.
[28] T.-F. Liu, D. Feng, Y.-P. Chen, L. Zou, M. Bosch, S. Yuan, Z. Wei, S. Fordham, K. Wang, H.-C. Zhou, J. Am. Chem. Soc. 137 (2015) 413–419.
[29] L. Liu, X.-N. Zhang, Z.-B. Han, M.-L. Gao, X.-M. Cao, S.-M. Wang, J. Mater. Chem. A 3 (2015) 14157–14164.
[30] S. An, J.S. Lee, B.N. Joshi, H.S. Jo, K. Titov, J.S. Chang, C.H. Jun, S.S. Al-Deyab, Y.K. Hwang, J.C. Tan, S.S. Yoon, J. Appl. Polym. Sci. 133 (2016) 1–8.
[31] B. Joshi, S. Park, E. Samuel, H.S. Jo, S. An, M.-W. Kim, M.T. Swihart, J.M. Yun, K.H. Kim, S.S. Yoon, J. Electroanal. Chem. 810 (2018) 239–247.
[32] J. Gao, X. Qian, R.B. Lin, R. Krishna, H. Wu, W. Zhou, B. Chen, Angew. Chemie Int. Ed. 59 (2020) 4396–4400.
[33] Y. Zhang, S. Yuan, X. Feng, H. Li, J. Zhou, B. Wang, J. Am. Chem. Soc. 138 (2016) 5785–5788.
[34] P. Kumar, K.-H. Kim, E.E. Kwon, J.E. Szulejko, J. Mater. Chem. A 4 (2016) 345–361.
[35] Y. Chen, S. Zhang, S. Cao, S. Li, F. Chen, S. Yuan, C. Xu, J. Zhou, X. Feng, X. Ma, B. Wang,Adv. Mater. 29 (2017), 1606221.
[36] F. Xie, N. Zhang, L. Zhuo, P. Qin, S. Chen, Y. Wang, Z. Lu, Compos. Part B Eng. 168 (2019) 406–412.
[37] T.-T. Li, L. Liu, M.-L. Gao, Z.-B. Han, Chem. Commun. 55 (2019) 4941–4944.
[38] T. Li, L. Liu, Z. Zhang, Z. Han,Sep. Purif. Technol. 237 (2020), 116360.
[39] Y. Bian, R. Wang, S. Wang, C. Yao, W. Ren, C. Chen, L. Zhang, J. Mater. Chem. A 6 (2018) 15807–15814.
[40] S. An, H.S. Jo, D.Y. Kim, H.J. Lee, B.K. Ju, S.S. Al-Deyab, J.H. Ahn, Y. Qin, M.T. Swihart, A.L. Yarin, S.S. Yoon, Adv. Mater. 28 (2016) 7149–7154.
[41] S. An, H.S. Jo, S.S. Al-Deyab, A.L. Yarin, S.S. Yoon,J. Appl. Phys. 119 (2016), 065306.
[42] H. Yoon, M.-W. Kim, H. Kim, D.-Y. Kim, S. An, J.-G. Lee, B.N. Joshi, H.S. Jo, J. Choi, S.S. Al-Deyab, Int. J. Heat Mass Transf. 101 (2016) 198–204.
[43] H.S. Jo, S. An, J.-G. Lee, H.G. Park, S.S. Al-Deyab, A.L. Yarin, S.S. Yoon, NPG Asia Mater. 9 (2017) e347.
[44] S. An, H.S. Jo, Y.I. Kim, K.Y. Song, M.-W. Kim, K.B. Lee, A.L. Yarin, S.S. Yoon, Nanoscale 9 (2017) 9139–9147.
[45] H.S. Jo, S. An, H.-J. Kwon, A.L. Yarin, S.S. Yoon, Sci. Rep. 10 (2020) 1–12.
[46] Y. Yun, H. Sheng, K. Bao, L. Xu, Y. Zhang, D. Astruc, M. Zhu, J. Am. Chem. Soc. 142 (2020) 4126–4130.
[47] E.P.V. Sánchez, H. Gliemann, K. Haas-Santo, W. Ding, E. Hansjosten, J. Wohlgemuth, C. Wöll, R. Dittmeyer,J. Memb. Sci. 594 (2020), 117421.
[48] L.S. Lai, Y.F. Yeong, N.C. Ani, K.K. Lau, A.M. Shariff, Part. Sci. Technol. 32 (2014) 520–528.
[49] B. Joshi, E. Samuel, Y.I. Kim, M.-W. Kim, H.S. Jo, M.T. Swihart, W.Y. Yoon, S.S. Yoon, Chem. Eng. J. 351 (2018) 127–134.
[50] E. Samuel, B. Joshi, M.-W. Kim, Y.-I. Kim, S. Park, T.-G. Kim, M.T. Swihart, W.Y. Yoon, S.S. Yoon, J. Power Sources 395 (2018) 349–357.
[51] S. Zhong, X. Yang, Z. Cao, X. Dong, S.M. Kozlov, L. Falivene, J.-K. Huang, X. Zhou, M.N. Hedhili, Z. Lai, Chem. Commun. 54 (2018) 11324–11327.
[52] A. Zukeran, Y. Ikeda, Y. Ehara, T. Ito, T. Takahashi, H. Kawakami, T. Takamatsu, Electr. Eng. Jpn. 130 (2000) 30–37.
[53] E. Kelly, D. Spottiswood, Miner. Eng. 2 (1989) 337–349.
[54] S. Sinha-Ray, S. Sinha-Ray, A.L. Yarin, B. Pourdeyhimi, J. Memb. Sci. 485 (2015) 132–150.
[55] J. Cravillon, C.A. Schröder, H. Bux, A. Rothkirch, J. Caro, M. Wiebcke, CrystEngComm 14 (2012) 492–498.
[56] J. Cravillon, R. Nayuk, S. Springer, A. Feldhoff, K. Huber, M. Wiebcke, Chem. Mater. 23 (2011) 2130–2141.
[57] M. Raffi, S. Mehrwan, T.M. Bhatti, J.I. Akhter, A. Hameed, W. Yawar, M.M. ul Hasan, Ann. Microbiol. 60 (2010) 75–80.
[58] Y. Zhang, Y. Jia, RSC Adv. 8 (2018) 31471–31477.
[59] K.S. Park, Z. Ni, A.P. Côté, J.Y. Choi, R. Huang, F.J. Uribe-Romo, H.K. Chae, M. O'Keeffe, O.M. Yaghi, Proc. Natl. Acad. Sci. (2006) 10186–10191.
[60] Y. Pan, Y. Liu, G. Zeng, L. Zhao, Z. Lai, Chem. Commun. 47 (2011) 2071–2073.
[61] A. Schejn, L. Balan, V. Falk, L. Aranda, G. Medjahdi, R. Schneider, CrystEngComm 16 (2014) 4493–4500.
[62] J. Cravillon, S. Münzer, S.-J. Lohmeier, A. Feldhoff, K. Huber, M. Wiebcke, Chem. Mater. 21 (2009) 1410–1412.
[63] M.J.C. Ordonez, K.J. Balkus Jr., J.P. Ferraris, I.H. Musselman, J. Memb. Sci. 361 (2010) 28–37.
[64] A. Jomekian, R. Behbahani, T. Mohammadi, A. Kargari, Microporous Mesoporous Mater. 234 (2016) 43–54.
[65] F. Bai, Y. Xia, B. Chen, H. Su, Y. Zhu, Carbon 79 (2014) 213–226.
[66] J. Liu, J. He, L. Wang, R. Li, P. Chen, X. Rao, L. Deng, L. Rong, J. Lei, Sci. Rep. 6 (2016) 23667.
[67] F. Yu, F. Li, B. Zhang, H. Li, L. Sun, ACS Catal. 5 (2015) 627–630.
[68] J. Wang, L. Zhu, L. Ji, Z. Chen, J. Mater. Res. 33 (2018) 581–589.
[69] Y. Huang, T. Zhao, G. Zhao, X. Yan, K. Xu, J. Power Sources 304 (2016) 74–80.
[70] N. Barka, S. Qourzal, A. Assabbane, A. Nounah, Y. Ait-Ichou, J. Photochem. Photobiol. A: Chem. 195 (2008) 346–351.
[71] P. Du, L. Song, J. Xiong, H. Cao, J. Mater. Sci. 48 (2013) 8386–8392.
[72] R. Kannan, D. Jayaraman, S. Aravindhan, Int. J. Sci. Eng. Appl. 4 (2015) 7–16.
[73] M. Okutan, R. Coşkun, M. Öztürk, O. Yalçın, Physica B Condens. Matter 457 (2015) 5–11.
[74] J. Zhao, T. Wu, K. Wu, K. Oikawa, H. Hidaka, N. Serpone, Environ. Sci. Technol. 32 (1998) 2394–2400.
[75] Y. Ho, G. McKay, Process. Saf. Environ. Prot. 76 (1998) 332–340.
[76] Y. Bian, S. Wang, L. Zhang, C. Chen,Build. Environ. 170 (2020), 106628.
[77] J. Wu, O. Akampumuza, P. Liu, Z. Quan, H. Zhang, X. Qin, R. Wang, J. Yu,Mater. Today Commun. 23 (2020), 100897.
[78] H. Liu, L. Liu, J. Yu, X. Yin, B. Ding,Compos. Commun. 22 (2020), 100493.
[79] A.C. Canalli Bortolassi, V.G. Guerra, M.L. Aguiar, L. Soussan, D. Cornu, P. Miele, M. Bechelany, Nanomaterials 9 (2019) 1740.
[80] J. Cao, Z. Cheng, L. Kang, M. Lin, L. Han, RSC Adv. 10 (2020) 20155–20161.
[81] C.-J. Cho, Y.-S. Chang, Y.-Z. Lin, D.-H. Jiang, W.-H. Chen, W.-Y. Lin, C.-W. Chen, S.-P. Rwei, C.-C. Kuo, J. Taiwan Inst. Chem. Eng. 106 (2020) 206–214.